

---

# Self-Calibrating BCIs: Ranking and Recovery of Mental Targets Without Labels

---

**Jonathan Grizou\***  
GrizAI

University of Glasgow  
jonathan.grizou@grizai.com

**Carlos de la Torre-Ortiz\***  
University of Helsinki

carlos.delatorreortiz@helsinki.fi

**Tuukka Ruotsalo**

LUT University  
University of Copenhagen  
tuukka.ruotsalo@lut.fi

## Abstract

We consider the problem of recovering a mental target (e.g., an image of a face) that a participant has in mind from paired EEG (i.e., brain responses) and image (i.e., perceived faces) data collected during interactive sessions without access to labeled information. The problem has been previously explored with labeled data but not via self-calibration, where labeled data is unavailable. Here, we present the first framework and an algorithm, **CURSOR**, that learns to recover unknown mental targets without access to labeled data or pre-trained decoders. Our experiments on naturalistic images of faces demonstrate that **CURSOR** can (1) predict image similarity scores that correlate with human perceptual judgments without any label information, (2) use these scores to rank stimuli against an unknown mental target, and (3) generate new stimuli indistinguishable from the unknown mental target (validated via a user study,  $N=53$ ). We release the brain response data set ( $N=29$ ), associated face images used as stimuli data, and a codebase to initiate further research on this novel task.

## 1 Introduction

We tackle the problem of recovering a mental target (e.g., an image of a face) that a participant holds in mind, using only unlabeled EEG responses (i.e., brain activity) recorded while the participant views a sequence of unlabeled images (i.e., perceived faces). These images, along with the mental target, are represented as high-dimensional vectors in the latent embedding space of a generative model. Thus, unlike traditional brain-computer interfaces (BCIs) that classify brain responses into a few discrete classes (e.g., yes/no or up/down/left/right), our task requires mapping EEG responses to distances in this high-dimensional space in order to recover the mental target iteratively. The challenge lies in probing these *continuous* high-dimensional spaces (image and EEG spaces) without discretizing them into labeled classes and only relying on paired data of image and brain representations.

Previous BCI methods that addressed this problem depended on labeled data or pre-trained decoders to map brain signals to a distance estimate [44]. In contrast, this paper introduces a method that requires no prior supervision, which makes it fully self-calibrating. Interestingly, self-calibrating BCIs (SC-BCIs) have been explored before but have been limited to tasks similar to P300 spellers with EEG decoded into discrete categories [28, 17, 23, 22, 43]. To our knowledge, this paper presents

---

\*equal contribution

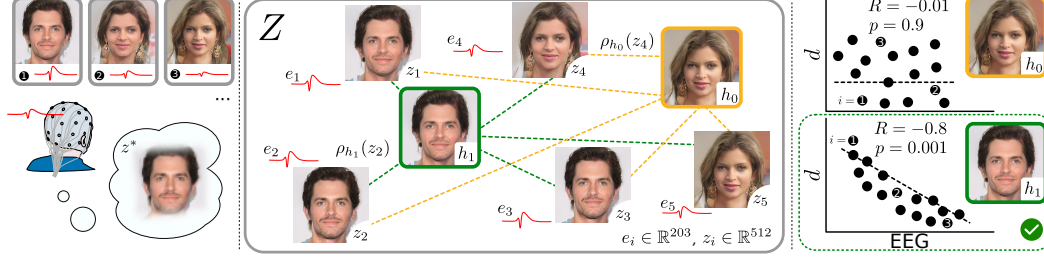


Figure 1: **(Left)** Participants are instructed to hold a mental target  $x^*$ , represented as  $z^*$ , unknown to our system, while a sequence of  $i = \{1, \dots, N\}$  images are shown to them and their EEG responses are being recorded. CURSOR’s goal is to recover  $z^*$  with this information alone and fully unsupervised. **(Middle)** CURSOR generates hypothetical target images, e.g.  $h_1$ , and builds a dedicated estimation problem to predict the distance  $d_i$  between  $h_1$  and  $z_i$  from the corresponding EEG response  $e_i$ , for all  $i$ . **(Right)** The performance of an estimator on this task is the score  $S(h_1)$  attached to  $h_1$ . The hypothesis with the highest score  $\hat{h} = \arg \max_{h \in \mathcal{H}} S(h)$  is assumed to be the unknown mental target. Images are generated from  $z_i \in \mathbb{R}^{512}$  embeddings with EEG responses  $e_i \in \mathbb{R}^{203}$ . We collected  $N = 9234 \{z_i, e_i\}$  pairs for this study from 29 participants.

the first SC-BCI framework for such continuous domains and demonstrates its effectiveness in a mental target recovery task.

To enable our study, we collected a large dataset ( $n=9234$ ) of EEG responses ( $\mathbb{R}^{203}$ ) recorded as participants ( $N=29$ ) viewed face images generated from a latent embedding space ( $\mathbb{R}^{512}$ ) while holding a mental target image in mind. Collecting novel data was necessary because existing datasets [12, 18] focus on categorization tasks with participants passively observing stimuli. Compared to existing datasets, ours is, to our knowledge, the only existing dataset suitable for this task because (1) stimuli are represented within a continuous space, (2) participants actively engage with a target in mind, (3) quantitative distance metrics between stimuli can be defined, and (4) ground-truth data for human distance judgment between two stimuli are obtained through a user study.

Equipped with a novel suitable dataset, we propose CURSOR (Consistency-based Unsupervised Regression for Similarity-based Optimization and Ranking), the first self-calibrating BCI algorithm for continuous domains. As illustrated in Figure 1, CURSOR first generates a hypothetical mental target as an embedding vector representing a face a user might have in mind. Given this hypothesis, CURSOR constructs a hypothesis-specific dataset that transforms observed faces into distances to this hypothetical target (Alg. 1, line 2). CURSOR then trains an estimator to decode EEG responses into these hypothetical distances, whose performance *relative to* the performance of an estimator trained on a deliberately misaligned dataset, is the CURSOR score for the hypothesis considered (Alg. 1, line 8). The CURSOR score should peak when evaluated at the (unknown) true mental target, because the EEG responses were recorded in that context and, therefore, should provide the strongest basis for predicting the corresponding distances.

CURSOR does not require access to any ground-truth supervision labels and thus solves the SC-BCI challenge. Our experiments confirm that CURSOR can identify the mental target a user has in mind from unlabeled EEG responses without requiring calibration, pre-trained decoders, heuristics, or labels. To our knowledge, this is the first work extending SC-BCIs to continuous domains. Our contributions are as follows:

1. We introduce the first SC-BCI framework and associated dataset for continuous domains.
2. We propose CURSOR, the first SC-BCI algorithm for continuous domains, supported by empirical validation across ranking and optimization tasks, allowing generating the mental image target and recovering ground truth labels.
3. We empirically analyze CURSOR’s performance under various conditions, including estimator type, data representation, and sensitivity to the amount of data.

## 2 Related Work

**BCI-driven visual decoding tasks.** We build on the established distinction between passive decoding (reconstructing viewed stimuli) and the active, iterative search of a mental image target [26]. In **passive EEG-guided generative decoding**, EEG is recorded while a participant views *unseen* images, and each signal is projected into a semantic latent space (e.g., CLIP or diffusion) from which a representative image is synthesized [4, 19]. The training uses time-aligned EEG–image pairs *without* category labels and can scale well with self-supervised objectives. Nevertheless, these methods typically generate an image from the target class rather than the *specific* stimulus instance (e.g., *some* face, not the exact face identity). Some works introduced fixed, block-structured stimuli resulting in temporal confounds that have been shown to inflate accuracy [2, 31, 1, 6]. Our approach avoids these confounds and does not belong to the passive decoding family.

For **iterative mental target search**, the system updates its estimate of the mental target based on preceding EEG responses, progressively steering the stimulus sequence toward a single mental target (e.g., a specific face image). Previous work relied on labeled target trials to learn the EEG-driven update rule and adapt the target estimate with heuristics based on binary labels [26] or distance estimates [44] decoded from EEG. Our method preserves the iterative search behavior of the latter while *eliminating the label requirement*, recovering a concrete target within a continuous high-dimensional generative manifold without pre-training data *or* ground-truth labels at any stage.

**SC-BCIs in classification contexts.** Self-calibrated BCI (SC-BCI) [22, 15] have been mostly developed for classification tasks. For instance, [28] relied on Expectation-Maximization (EM), assuming signals can be linearly projected onto two one-dimensional Gaussian distributions (yes/no responses) and aiming to maximize the distance between these distributions. Later designs used classification accuracy on datasets attached to each possible target as a scoring metric [17, 23], which [40, 43] approximated using the distances between the mean of two classes. Label proportion (LP), initially proposed by [37], was applied to BCIs by [21]. LP assumes a known, unbalanced ratio of labels in stimuli-response pairs that can be exploited to label clusters identified from unsupervised clustering methods. Further work has extended LP to reinforcement learning [51] from unlabeled reward to break symmetry after applying contrastive learning, and [46] explored the combination of EM and LP methods.

Self-calibration was also explored in Human-Robot Interaction [16], Human-Computer Interfaces [38, 15, 50], Security and Privacy [32] and Language Games [47, 5], always in a classification context.

## 3 Self-calibration Problem Formulation

We consider interaction sessions as pairs of stimuli and responses, where stimuli are images of faces  $x \in X$ , represented as embedding vectors  $z \in Z$  from a known generative model  $G : Z \mapsto X$ . We rely on the same model to collect paired  $(x, z)$  for simplicity, but other methods could be used to generate and embed stimuli, respectively, which could be part of future research. User responses are EEG signals  $e \in E$ , recorded post-stimuli. Interaction sessions of length  $N$  are captured by stimuli-response pairs  $\Psi_N = \{(z_i, e_i)\}_{i=1}^N$ . During interactions, participants guide the system by mentally focusing on a target  $x^*$ , represented as  $z^*$  and unknown to the algorithm, while they observe a sequence of stimuli  $x_i$ , represented as  $z_i$ . The aim is to estimate  $\hat{z}$  that approximates  $z^*$  using  $\Psi_N$ .

**Similarity equivalence.** Participants observe only  $x_i$  without explicit knowledge of  $Z$ , but we know EEG responses  $e_i$  encode perceptual similarities in  $X$ , correlating with distances  $d_i$  in  $Z$  [45]. In other words, EEG responses  $e_i$  do not encode  $z^*$  directly but “how far”  $z$  is from  $z^*$ . This implies the existence of a function  $f_{\theta_{z^*}} : E \mapsto \mathbb{R}^+$  mapping EEGs  $e_i$  to distances  $d_i$  in  $Z$ , although it is not directly accessible. Similarly, we assume the existence of a similarity function  $\rho_{z^*} : Z \rightarrow \mathbb{R}^+$  that returns a distance  $d_i$  between a mental target  $z^*$  and an observed stimulus  $z_i$ . Hence:

$$f_{\theta_{z^*}}(e_i) = d_i = \rho_{z^*}(z_i) \quad (1)$$

with  $z^*$ ,  $\theta_{z^*}$ ,  $d_i$ ,  $\rho_{z^*}$  unknown but access to  $(e_i, z_i)$  pairs.

**Error estimation.** According to Equation 1, the task reduces to identifying  $\hat{z}$  that minimizes the error between our two estimates  $f_{\theta_{\hat{z}}}(e_i)$  and  $\rho_{\hat{z}}(z_i)$ , based on observed  $(z_i, e_i)$  pairs in  $\Psi_N$ . This can

be measured on the entire dataset by defining an error-based score such as:

$$\hat{z} = \arg \min_z \sum_{i=1..N} ERROR(f_{\theta_z}(e_i), \rho_z(z_i)) \quad (2)$$

where  $ERROR()$  is a metric function defined to best suit the problem.

The SC-BCI challenge lies in the reciprocal dependency between  $\theta_z$  and  $\rho_z$ . Both are apriori unknown and need to be learned. But to learn  $\theta_z$ , we need access  $\{e_i, d_i\}$  pairs, which can only be acquired by knowing  $\rho_z$  to reconstruct  $d_i$  based on  $z_i$ ; and vice versa, to learn  $\rho_z$ , we need  $\theta_z$ .

## 4 CURSOR Algorithm

CURSOR, our proposed algorithm, solves this SC-BCI challenge by (1) defining a similarity function  $\rho_z$  for any  $z$ , which allows us to break the dependency deadlock in Equation 2; (2) defining an  $ERROR$  function that controls for the variability between datasets generated via  $\rho_z$ ; and (3) searching the hypothesis space of mental targets  $Z$  guided by the  $ERROR$  scores.

In the following, we use  $h \in Z$  as a hypothetic mental target to be evaluated in Equation 2. We use  $h$  to differentiate hypotheses from observations  $z_i$  clearly, ground truth mental target  $z^*$ , and best estimate  $\hat{z}$ , which all exist in  $Z$ .

**(1) Defining a similarity function.** We define  $\rho_h(z_i) = \|h - z_i\|_2$ , which we assume to be valid for any hypothesis target  $h$  and any observed stimuli  $z_i$ . This choice reflects the assumption that the perceptual similarity between an observed image  $z_i$  and a target image  $\hat{z}$ , as encoded in their EEG responses, correlates linearly with Euclidean distances in the structured latent space  $Z$ , in agreement with the findings of [45]. Knowing  $\rho_h$  allows the estimation of Equation 2 by breaking the reciprocal dependency between  $\theta_h$  and  $\rho_h$  for a given  $h$ . We use  $\rho_h(z_i)$  to build a first estimate of  $d_i$ , which in turn can be used to estimate  $\theta_h$  via  $(e_i, d_i)$  pairs.

**(2) Defining a  $ERROR$  function.** Given  $\rho_h(z_i)$ , we construct a dataset  $\Gamma_N^h = \{(e_i, d_i^h)\}_{i=1}^N$  associated to  $h$  where  $d_i^h = \rho_h(z_i)$  (Alg. 1, line 2). With this dataset, we can estimate  $\theta_h$  by training an estimator on  $\Gamma_N^h$ . Equipped with both  $f_{\theta_h}$  and  $\rho_h$ , we can rely on well established error metrics for Equation 2, such as  $RMSE(f_{\theta_h}(e), \rho_h(z))$ , where lower values indicate stronger predictability.

However, comparing RMSE scores directly is unsuitable because the distribution of  $d$  values in  $\Gamma_N^h$  will vary between hypothesis  $h$ , even post-standardization. For example, a hypothesis  $h_f$  “far away” from all observed  $z_i$  would lead to a narrow distribution of  $d_i^{h_f}$ , which is highly predictable. Hence, an RMSE score based on  $\Gamma_N^{h_f}$  could compare favorably even with respect to the ground truth dataset  $\Gamma_N^{z^*}$ .

To standardize errors across datasets, we compute a *relative gain* against a baseline score computed from misaligned stimuli-response pairs of the same dataset. In practice, a permutation  $\sigma$  produces a shuffled dataset  $\Gamma_{N,\sigma}^h$  (Alg. 1, line 5). The final CURSOR score  $S(h)$  is defined by the ratio of the respective RMSE scores (Alg. 1, line 8) as:

$$S(h) = \frac{RMSE(f_{\theta_{h,\sigma}}(e_\sigma), \rho_h(z))}{RMSE(f_{\theta_h}(e), \rho_h(z))} = \frac{\|f_{\theta_{h,\sigma}}(e_\sigma) - \rho_h(z)\|_2}{\|f_{\theta_h}(e) - \rho_h(z)\|_2}$$

with  $S$  a relative error-ratio function which is to be maximized so  $\hat{h} = \arg \max_h S(h)$ .

**(3) Searching the hypothesis space.** CURSOR scores can be used in downstream tasks such as ranking and optimization. Indeed, hypotheses  $h$  do not need to be among observed stimuli or within a fixed test set, allowing any stimulus representation in  $Z$  to be scored, thus allowing  $S$  to guide an optimization process throughout the latent space. Evaluation frameworks are detailed in Section 6.2

## 5 Neurophysiological Data Acquisition

To run our experiments, a dataset of artificial human face images and associated EEG responses was collected from 31 participants, with 2 dropped due to data corruption.



---

**Algorithm 1** CURSOR: Scoring Function

---

<b>Require:</b> Stimuli-response dataset $\Psi_N = \{(z_i, e_i)\}_{i=1}^N$	1: <b>function</b> $S(h)$
<b>Require:</b> Target hypothesis $h \in \mathcal{Z}$	2: Construct hypothesis dataset $\Gamma_N^h = \{(e_i, d_i^h)\}_{i=1}^N$
<b>Require:</b> Similarity function $d_i^h = \rho_h(z_i) = \ h - z_i\ _2$	3: Train estimator $f_{\theta_h}$ on $\Gamma_N^h$
<b>Require:</b> Estimator $f_\theta : E \rightarrow \mathbb{R}^+$	4: Compute $\text{RMSE}_h = \text{RMSE}(f_{\theta_h}(e), d^h)$
<b>Require:</b> Error function $\text{RMSE}(\hat{y}, y^*) = \frac{1}{\sqrt{N}} \ \hat{y} - y^*\ _2$	5: Generate shuffled dataset $\Gamma_{N,\sigma}^h = \{(e_{\sigma(i)}, d_i^h)\}_{i=1}^N$
	6: Train shuffled estimator $f_{\theta_{h,\sigma}}$ on $\Gamma_{N,\sigma}^h$
	7: Compute shuffled $\text{RMSE}_{h,\sigma} = \text{RMSE}(f_{\theta_{h,\sigma}}(e_\sigma), d^h)$
	8: <b>return</b> $\text{RMSE}_{h,\sigma} / \text{RMSE}_h$

---

**Generating stimuli for the experiment.** A pretrained GAN [13] on the CelebA-HQ dataset [27]<sup>2</sup> was used to generate stimuli images. The GAN maps its latent space  $Z$  to the image space  $X$  as  $G : Z \mapsto X$ . We sampled the generator using 512-dimensional Gaussian noise to produce images and selected 17 target images without visual artifacts, represented by  $z_t^*$  latent vectors. For each target, stimuli were generated at logarithmically spaced Euclidean distances in  $Z$ , ranging from 0 to 46.16. Images were sampled along one trajectory in the latent space to ensure smooth and predictable transitions between stimuli. This logarithmic sampling aligns with neuroscientific methodologies for studying perceptual thresholds and neural adaptation. Mitigations for these biases in the machine learning experiments are described in the following sections.

**EEG processing and dataset.** Subjects were asked to make a mental note of the target. Images at various similarity distances from the target were presented with an RSVP design at 500 ms intervals, aiming to evoke a P3-like response. EEG was recorded using a 32-channel EasyCap system (29 effective channels after removing corrupted ones) and signals were processed offline using MNE for Python [14]. Standard filtering, time-locking into “EEG epochs,” and artifact rejection were applied. Temporal EEG data was windowed into 7 equidistant time windows within the 50–800 ms range after stimulus onset. Our final dataset consists of 9234 stimuli-response pairs, with each entry composed of a  $z_i^*$  vector in  $\mathbb{R}^{512}$ , a stimuli  $z_i$  vector in  $\mathbb{R}^{512}$ , and an EEG response vector  $e_i$  in  $\mathbb{R}^{203}$ . **The complete details of the EEG experiment can be found in Appendix A.**

## 6 Experiments

We evaluated CURSOR’s ability to rank and optimize facial stimuli against an unknown mental target based on unlabeled EEG responses. We describe our experimental framework, dataset preparation, and comparative studies, including ablations and control conditions. In addition, we validated our approach through human perception studies.

### 6.1 Datasets preparation for simulation runs

Not all stimuli-response pairs in the dataset were collected with the same target face  $z^*$ . To enable our study, we generated equivalent datasets, each with a single target face  $z^*$ , by generating new stimuli in the latent  $Z$ -space that preserved the original statistical properties. We used gradient descent, starting from a randomly sampled 512-dimensional starting point, to match the Euclidean distance from the original dataset to the new target. We created 10 dataset variants for each of the 17 target faces utilized in our neurophysiological experiments, yielding 170 stimuli-response datasets that preserved the original statistical properties.

For ranking tasks, we built separate hypothesis sets of  $L = 60$  faces for each of the 17 target faces. Each hypothesis  $h_l$  is generated at distance  $d_l$  from the target, with  $d_l$  sampled uniformly in  $[0, 46.16]$ . 46.16 being our dataset’s maximum  $d$  value, ensuring our evaluation is within observed bounds.

### 6.2 Evaluation frameworks

Our study faces computational challenges due to high-dimensional data: stimuli (image embedding representation) in  $\mathbb{R}^{512}$  and responses (flattened EEG representations) in  $\mathbb{R}^{203}$  making search a

---

<sup>2</sup>Pre-trained model and code: [https://github.com/tkarras/progressive\\_growing\\_of\\_gans](https://github.com/tkarras/progressive_growing_of_gans)

difficult process without a large sampling budget. Evaluating  $S$  is also computationally intensive, requiring cross-validation training of estimators on the 203D response space at each iteration. The need for multiple runs, baselines, and ablation studies compounds these challenges. We thus adopted a two-stage evaluation approach: ranking a predefined set of hypotheses and then optimizing in dimensionally-reduced spaces.

**Unsupervised hypotheses ranking.** For ranking evaluations, we assume the system has access to a finite set of  $L$  hypotheses  $\mathcal{H} = \{h_1, \dots, z^*, \dots, h_L\}$ , which allows us to compute score on a finite set of candidates. To simplify the interpretation of results, we included the mental target  $z^*$  in  $\mathcal{H}$  which guarantees the oracle baseline of the “similarity to top rank” metrics is 0 on Figure 3 right. This is by no means a requirement of our approach as we also demonstrate optimization results on dimensionally reduced spaces (see Figure 4). We rank the hypotheses directly by their CURSOR’s scores, breaking ties randomly. The following metrics are then evaluated:

- **Score-distance correlation.** Pearson’s correlation coefficient  $R(S(h), \rho_{z^*}(h))$  between CURSOR scores and ground-truth target distances.
- **Target rank.** The rank of the target stimuli as measured by  $\text{rank}(z^*) = \sum_{h \in \mathcal{H}} \mathbb{I}(S(h) \geq S(z^*))$  where  $\mathbb{I}(\cdot)$  is the indicator function.
- **Similarity at top rank.** We report the similarity of the best ranked hypothesis to the ground-truth target as  $\rho_{z^*}(\hat{h})$ .

**Optimizing with dimensionality reduction.** To demonstrate the feasibility of optimizing a target stimulus based on our scoring function  $S$ , we reduced the dimensions of  $e$  for faster score calculation and of  $z$  for faster convergence. We applied Principal Component Analysis (PCA) to reduce  $e$  to  $\mathbb{R}^{20}$  and  $z$  to  $\mathbb{R}^{10}$ , with Appendix B detailing our rationale with computational evidence. We conducted optimization experiments in these reduced spaces. Covariance Matrix Adaptation Evolution Strategy [20], implemented via Optuna [3] using default parameters, was chosen for optimization due to the high-dimensional, gradient-free nature of our problem. Optimization bounds were set to  $[-15, 15]$  per reduced dimension, corresponding to maximum distances in the 512D space that align with our ranking experiments (47.42 vs 46.16), allowing a fair comparison between ranking and optimization performance. We report the similarity of the optimized stimuli with the ground truth target  $\rho_{z^*}(\hat{h})$  projected back to the original  $Z$  to allow a meaningful comparison with the ranking and human-experiment results.

### 6.3 Comparative and ablation studies

For a comprehensive evaluation, we evaluated the impact of different estimator models, included two control conditions, ran multiple data scarcity scenarios, and tested with two EEG signal representations. The computational environment is detailed in Appendix C.3.

**Estimators.** Our method requires training estimators  $f_{\theta_h}$  on  $\Gamma_N^h$  to compute  $S(h)$ . We compared performance using Linear Regression (LR), Support Vector Regression (SVR), and Multi-Layer Perceptron (MLP) as implemented in Scikit-learn library [35]. The relative model simplicity allows for a rigorous evaluation with cross-validation and hyperparameter optimization setups within our computational resources. In addition, linear models are known to perform particularly well in EEG tasks [34, 42, 8, 30, 7]. When training estimator parameters  $\theta$ ,  $e$ , and  $d$  are standardized by removing the mean and scaling to unit variance for each feature. Each  $S(h)$  estimate is the average of a 10-fold 90%/10% randomly partitioned cross-validation procedure. As detailed in Appendix C.1, we decided not to pre-tune estimators’ meta-parameters using ground-truth information because our approach is meant to be fully unsupervised, and doing so would not represent a realistic SC-BCI scenario. Nonetheless, we assessed the performance of SVR and MLP with offline hyperparameter optimization, which we detail in Appendix E.1.

**Control conditions.** We benchmarked CURSOR using theoretically ineffective estimators for computing  $S(h)$ . Our control conditions include: 1) a dummy estimator (*Dummy*) predicting  $d$  as the average of all distances in  $\Gamma_N^h$  without considering  $e$ , and 2) a Linear Regressor that always Shuffle stimuli and response pairs prior to training (*S-LR*). Both baselines should perform at chance level, confirming that our algorithm’s information gain comes solely from EEG responses. For ranking,

results are compared to random guessing. For  $L = 60$  candidates, the average target rank is 30, and the expected  $d$  of a top-ranked face is 23.08.

**Data and distance ablations.** We evaluated our algorithm with varying dataset sizes ( $n$ ) from 100 to 9234 to assess performance impact. Each dataset size was produced via uniform random sampling in  $\Gamma_N$  without replacement. We also tested sensitivity to near-target stimuli by removing stimuli-response pairs below distance thresholds from the target face (0 to 40), reducing dataset sizes from 9234 to 806. We ran parallel experiments with uniformly down-sampled datasets matching each threshold’s size to control for dataset size effects. Further details can be found in Appendix C.1.

**Alternative EEG representations.** To follow the representation learning with linear model evaluation framework [49, 33], we re-ran most experiments using EEGNet embeddings of the raw EEG responses, which has shown state-of-the-art performance in many tasks [29]. EEGPT [48] is a more recent, promising, self-supervised pre-trained EEG representation but was published after our experiments had ended. While our contribution lies not in representation learning but in an SC-BCI framework that can be applied to any representation, future research could focus on comparing performance between various EEG representations. Additionally, we leveraged alternative representations to ensure open reproducibility, employing EEGNet to bypass limitations on sharing our original dataset imposed by privacy constraints. This enables the sharing of encoded data openly. An EEGNet model from Braindecode [39] was trained on a separate dataset specifically for task-relevant P3 classification. Further details and EEGNet results are in Appendix D.

## 6.4 Human validation experiments

We conducted two user studies to ground our results against human perceptual judgments. First, via ***H-Rank***, where a user manually scored image similarity to compare the algorithm’s scores with fine-grained human perception. Second, via ***H-ID***, where a larger cohort determined the distance at which humans stop perceiving differences between faces. This second study contextualized all downstream experiments without requiring individual experiments for each scenario. Participants and precise experimental details can be found in Appendix C.2.

## 7 Results

**How algorithm and human scores correlate with the similarity function.** Figure 2 (left) shows that, in a randomly selected experimental run, CURSOR scores exhibit a strong negative correlation with the distance between the hypothesis and target faces, showing a Pearson coefficient  $R$  of -0.82 ( $p < 0.001$ ). These scores also align closely with those manually assigned by human evaluators, achieving an  $R$  of -0.97 ( $p < 0.001$ ). This outcome confirms that CURSOR and *H-Rank* scores match effectively, correlating well with our similarity metric.

**How human identification rate varies with image distances.** *H-ID* results (Figure 2 — right) confirmed near-chance identification at distances close to zero with  $\eta(0) = 0.493$  (95% CI: 0.414, 0.573) and  $\eta(1.6) = 0.503$  (95% CI: 0.425, 0.581) indicating perceptual indistinguishability for  $d \leq 1.6$ . At  $d \geq 16.3$ , faces became clearly distinguishable with  $\eta(16.3) = 0.037$  (95% CI: 0.018, 0.074).

**How unsupervised ranking of images match their similarity to the mental target** The predicted scores were utilized to rank hypotheses by their similarity to the mental target, with the Linear Regressor (LR) performing best across all metrics (Figure 3 and Table 1). The average correlation coefficient between predicted scores and ground-truth distances was  $-0.77 \pm 0.04$  SD for LR, indicating that predicted scores effectively rank the hypotheses, with a mean top rank of 6.64 out of 60. At the top rank, our method achieved a mean distance of  $2.9 \pm 3.08$  SD to the unknown target face, a distance only slightly perceptible to human subjects  $\eta(3.6) = 0.377$  (95% CI: 0.304, 0.455).

Baseline performance was significantly worse than LR across all metrics (Mann-Whitney U,  $p < 0.001$ , Bonferroni corrected), with a significant perceptual difference of top ranked faces to the target (Fisher exact test comparing  $\eta(3.6)$  and  $\eta(21.7)$ , odds ratio = 18.49,  $p < 0.001$ ), confirming that EEG responses are the source of information and CURSOR unsupervised scoring function can convincingly rank hypothetical targets.

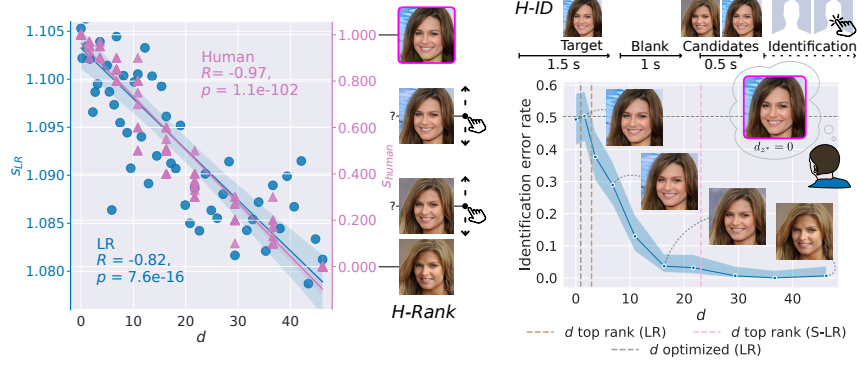


Figure 2: **(Left)** CURSOR and human scores correlate strongly with similarity. [Blue] Predicted scores ( $S$ ) (Alg. 1 with LR estimator using full dataset) against ground-truth similarity ( $d$ ) for 60 face images with regression lines and 95% ci. [Pink] Human-assigned  $H$ -Rank scores to sets of 10 facial images morphing away from the target [right axis]. **(Right)** A face at  $d \leq 1.6$  has an error rate at chance level, suggesting perceptual indistinguishability to the target. A stimulus at  $d \geq 16.3$  has an error rate nearing 0, confirming perceivable differences from the target. These statistics (Wilson Score shading at 95% ci) were collected during  $H$ -ID trials [top]. The vertical dotted lines show ranking and optimization performance, both recovering faces indistinguishable from the target.

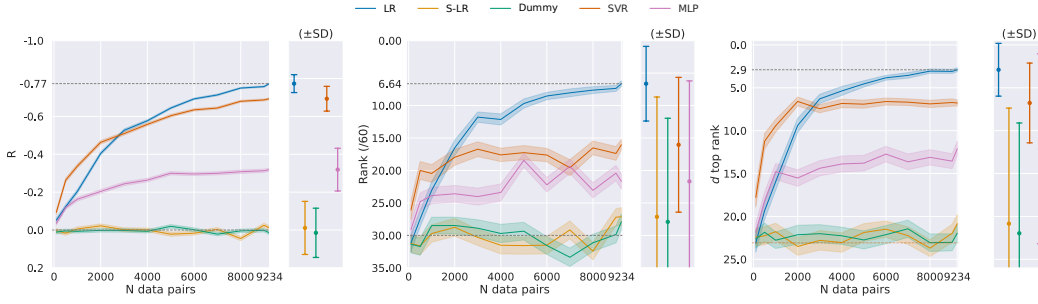


Figure 3: Rank-related performance for different estimators and data sizes (mean  $\pm$  ste, std at  $N$ , inv. y-axis). **(Left)** Correlation coefficient ( $R$ ) between scores and ground-truth distances. **(Middle)** Target rank out of 60. **(Right)** Euclidean distance to the target for top ranked candidate. The bottom dotted line is theoretical random performance. With LR rankings, human subjects could barely distinguish top-ranked faces from the target face with  $\eta(3.6) = 0.377$  (95% CI: 0.304, 0.455).

Table 1: LR scores best across metrics, with LR, MLP, and SVR metrics significantly better than S-LR and Dummy controls (Mann-Whitney U,  $p < 0.001$ , Bonferroni corrected). The table shows ranking metrics (mean  $\pm$  std) of different estimators and baselines at  $N=9234$  in Figure 3.

Model	R	Rank	$d$ top rank
<b>LR</b>	<b>-0.77 <math>\pm</math> 0.04</b>	<b>6.63 <math>\pm</math> 5.75</b>	<b>2.90 <math>\pm</math> 3.08</b>
S-LR	-0.01 $\pm$ 0.14	27.13 $\pm$ 18.45	20.85 $\pm$ 13.48
Dummy	0.01 $\pm$ 0.13	27.91 $\pm$ 15.95	21.97 $\pm$ 12.86
MLP	-0.32 $\pm$ 0.11	21.68 $\pm$ 15.48	12.11 $\pm$ 11.07
SVR	-0.69 $\pm$ 0.06	16.04 $\pm$ 10.38	6.77 $\pm$ 4.65

**How ranking performance varies across estimators and data sizes.** The performance of comparison estimators, SVR and MLP, was consistently lower than the Linear Regressor but above the control conditions, confirming that our algorithm works as long as the estimator used can improve prediction performance over shuffled versions of the dataset. We investigated estimators' performance on labeled data versus their performance on this task in more detail in Appendix E.2. Based on these results, and given that LR is faster to fit, we used only LR for the optimization tasks along with our two baselines (S-LR and Dummy).

**How optimization performs in dimensionally reduced spaces.** The optimization process successfully converged to an optimal face (Figure 4), positioned at an average Euclidean distance of 0.93 from the unknown target face in the original latent space — a difference barely perceptible to human subjects with  $\eta(1.6) = 0.503$  (95% CI: 0.425, 0.581). In contrast, the control methods S-LR and Dummy failed to converge, yielding faces at average Euclidean distances of 24.09 and 22.51 from the target face, which are clearly perceptible to human subjects with  $\eta(21.7) = 0.014$  (95% CI: 0.072, 0.032).

Baselines performance is significantly worse than LR (Mann-Whitney U,  $p < 0.001$ , Bonferroni corrected), with a significant perceptual difference (Fisher exact test comparing  $\eta(1.6)$  and  $\eta(21.7)$ , odds ratio = 31.00,  $p < 0.001$ ), confirming that EEG responses are the source of information and CURSOR unsupervised scoring function can successfully guide an optimization process.

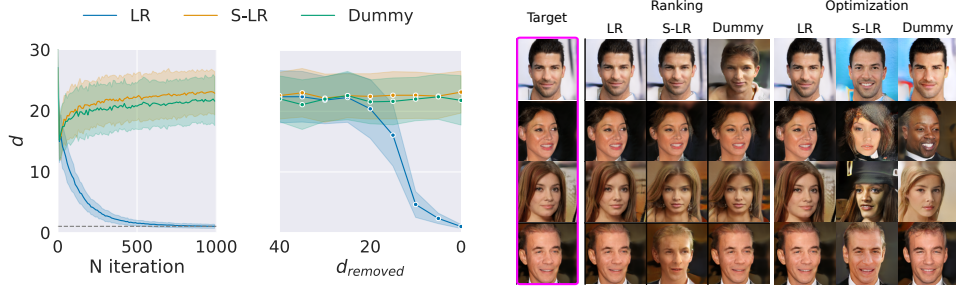


Figure 4: **(Left)** Optimization converges to  $< 1$  distance to the target. Candidates distance ( $d$ ) to the target against iteration number (left, mean  $\pm$  std). We can recover near-target faces even when near-target stimuli are absent in the dataset, up to  $d_{removed} = 10$ . Best candidates found after 1000 iterations shown against ablation distances  $d_{removed}$  around the target (right, mean  $\pm$  std). **(Right)** Top-ranked (middle) and optimized (right) images per estimators from one randomly selected run and four randomly selected target faces (left). Images from CURSOR using Linear Regression (LR) are indistinguishable from the target image, while controls S-LR and Dummy exhibit visual differences.

**Visual inspection.** Figure 4 (right) shows top-ranked and optimized faces for randomly selected runs and target faces between our best estimator (LR) and controls. Images for all 17 targets are included in Appendix Figure 10.

**Recovering ground-truth labels.** Once  $\hat{z}$  has been recovered in an unsupervised manner, we can reconstruct each distance via  $\hat{d}_i = \rho_{\hat{z}}(z_i)$  for all  $z_i \in \Psi_N$ . Appendix E.6 shows that these reconstructed distances closely match the ground-truth distances and are significantly more accurate than those produced by all baseline methods.

## 8 Discussion, Limitations, and Conclusions

We addressed the problem of recovering image targets that a participant has in mind using only unlabeled EEG responses recorded while viewing a sequence of unlabeled images. Unlike previous BCI-driven visual decoding tasks that rely on labeled data and/or map brain signals onto discrete categories, our self-calibrating approach iteratively searches a continuous high-dimensional latent space guided only by unlabeled brain responses. We demonstrated that our CURSOR algorithm can address this problem, recovering images indistinguishable from the targets participants had in mind, as confirmed by a user study ( $N = 53$ ).

**Dataset contribution.** To our knowledge, we release the first EEG dataset ( $n=9234$ ) for exploring SC-BCI in continuous domains with stimuli represented in a latent space and participants actively engaging with a target in mind.

**Limitations.** This study is restricted to face stimuli from one pre-trained GAN, the acquisition protocol never explored latent distances  $> 40$  (Euclidean) from the target, and relied on a predefined similarity function in the stimuli latent space. The optimization was run in a lower-dimensional latent subspace chosen for computational efficiency, which may bias optimization. Real-time performance and cross-subject generalization remain untested.

**Broader impact.** Ethical considerations are critical as inferring intent without explicit consent raises privacy concerns [9, 11]. Working on explainable SC-BCIs and methods to assess confidence in their predictions will play a crucial role. The technology could broaden access to communication for users who cannot provide reliable overt feedback (e.g., individuals with severe motor impairments) and open new forms of adaptive human-computer interaction. Future work should pursue such benefits while remaining vigilant about misuse.

## Appendix

### A Neurophysiological Data Acquisition

**Participants.** The Ethical Committee of ANONYMOUS INSTITUTION approved the study protocol, and participation in the neurophysiological experiment was advertised to a university population. In total, 31 participants volunteered for the study, aged  $23.5 \pm 3.5$  (mean  $\pm$  SD), from which 13 self-identified as male, 18 as female, and none as diverse. All participants were informed of the study’s purpose and provided written consent before participation. After completing the study, participants were compensated with cinema vouchers.

**RSVP task** Subsequently, the Rapid Serial Visual Presentation (RSVP) block started, presenting one facial image at a time every 500 ms using E-Prime 3 [41]. To minimize visual variance unrelated to facial features, a gray ellipsoid mask of  $746 \times 980$  pixels was applied to each image. Each trial included 70 images: 28.5% related images and 71.5% unrelated images, where the imbalance is intended to enable the “oddball” paradigm. This design avoids confounds arising from participants attempting to predict the following image. It also facilitates the processing of data into overlapping epochs, therefore balancing acquisition speed with data quality [10]. The order of the images was randomized for each trial but ensuring that each presentation of a related image was followed by 1 to 8 unrelated images. In total, each participant completed 16 trials, therefore displaying 1120 images generated from the 16 image targets. Data acquisition sessions, including setup and EEG recording, lasted approximately one hour.

The participants received the following instructions before starting the task:

In this block you will be asked to concentrate and  
mentally count every time you see this person below.  
[Source image shown: young dark-haired female]  
[Participant clicks the image]

That means you should ignore people who are not this person.  
For example, ignore people such as this:  
[Flanker image shown: young blond female,  
different identity than source]  
[Participant clicks the image]

Pictures of persons will be shown.  
If the person is the one now shown in the middle, count it.  
If the person looks different  
(e.g. like the ones on the side), ignore it.  
Click on the middle picture to begin!  
[Three images shown: flanker, source, flanker;  
same respective identities as before]  
[Participant clicks the central image]

You will be shown faces.  
Silently count the relevant ones.  
Press SPACE to begin

[RSVP begins]  
[Three images: flanker (constant),  
changing image, flanker (constant)]  
[70 central images shown]

How many did you count?  
You will receive a prize if your  
count is closest to the correct answer!  
[Text input field]  
[Participant types the count]

Thank you for participating and goodbye!  
The experiment will close in 4 seconds.

**EEG recording.** The experimental setup used a 32-channel EasyCap system, utilizing Ag/AgCl electrodes in the 10-20 system placed at FP1, FP2, F7, F3, Fz, F4, F8, FT9, FC5, FC1, FC2, FC6, FT10, T7, C3, Cz, C4, T8, TP9, CP5, CP1, CP2, CP6, TP10, P7, P3, Pz, P4, P8, O1, O2, and Iz, with AFz as ground. The participants seated at approximately 60 cm away from a 24" LCD screen with a resolution of  $1920 \times 1080$  pixels and a refresh rate of 60 Hz.

The EEG responses were captured utilizing a BrainProducts QuickAmp USB amplifier, with voltages digitized via BrainVision Recorder at a sampling rate of 1000 Hz and using 0.01 Hz high-pass filter. During recording, signals were re-referenced to the common average. Electrooculographic (EOG) signals were recorded using bipolar electrodes, positioned in the peripheral area surrounding both eyes. Specifically, one pair was placed laterally to both eyes, while another pair was positioned above and below the right eye. The resulting signals are a time series of voltages distributed across channels in an  $e \times c \times t$  tensor (EEG events, 32 channels, time).

**EEG filtering and artifact rejection.** EEG responses were processed offline using MNE for Python [14]. Signals were filtered using a 0.1 Hz high-pass filter and a 50 Hz low-pass filter. Then segmented into time-locked bands, or *epochs*, each lasting 1 s and starting 0.2 s prior to the onset of each image stimulus [10]. Epochs were then baseline-corrected by subtracting the mean voltage per channel.

Artifact rejection was performed by eliminating epochs with a voltage exceeding  $\pm 400 \mu$  in channels F3, Fz, F4, FC1, FC2, C3, Cz, C4, CP1, CP2, P3, Pz, and P4. Following, they applied Independent Component Analysis (ICA) to remove further artifacts such as eye movements. For this, they employed Autoreject [24, 25], resulting in a 5.3% epoch rejection rate. To expedite downstream computations, EEG responses were finally resampled to 250 Hz. Unlike its default behavior, Autoreject was configured to drop defective epochs rather than repair them. Channels with data corruption were dropped across all participants, reducing the number of channels from 32 to 29.

The resulting  $e \times c \times t$  tensor (EEG events, 29 channels, time) was then standardized to zero mean and unit variance across trials for each participant, and across participants, to reduce inter-trial and inter-participant variability. EEG was windowed into seven equidistant time windows between 50 ms and 800 ms post-stimulus onset to streamline further and denoise the data. This yields an  $e \times c \times w$  (EEG events, 29 channels, 7 time windows) tensor (i.e.  $29 \times 7 = 203$  features per EEG event). CURSOR used flattened representations of the resulting EEG tensor, concatenated with image embeddings.

## B Optimizing with Dimensionality Reduction.

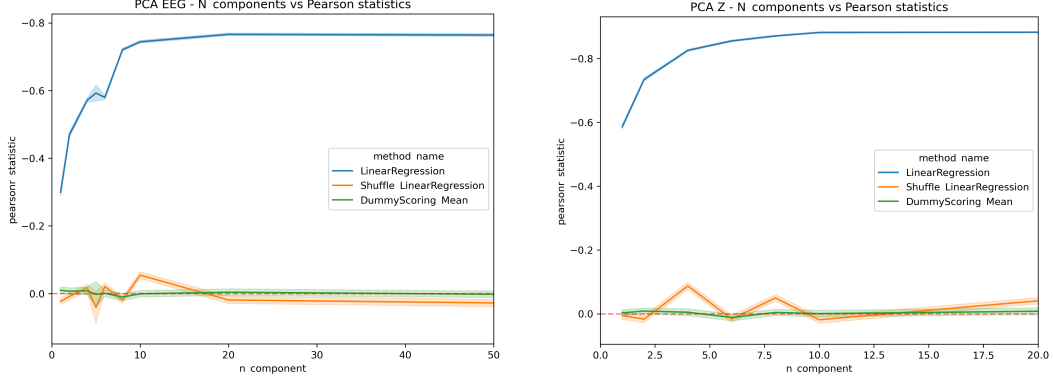
The selection of appropriate dimensionality for PCA reduction was guided by the analysis of Pearson correlation statistics across varying numbers of principal components. Figures 5a and 5b illustrate the justification for our choices of 20 and 10 dimensions for EEG and face embedding reduction, respectively.

**EEG Dimensionality Reduction.** Figure 5a displays the relationship between the number of PCA components and the Pearson correlation statistic in ranking experiments. Linear Regression method demonstrates gradual improvement that plateaus around 20 components. This asymptotic behavior suggests that 20 dimensions capture the majority of the relevant variance in the EEG data.

**Face Embedding Dimensionality Reduction.** Similarly, Figure 5b presents the PCA analysis for face embeddings. Linear Regression method demonstrates gradual improvement that plateaus around 10 components. This indicates that a 10-dimensional representation is sufficient to retain most of the informative features of the face embeddings.

In both cases, the control estimators (Dummy and S-LR) consistently showing little to no correlation across all component numbers, hence no leakage of information despite significant dimensionality reduction.





(a) Dimensionality reduction of EEG via PCA. The Linear Regression method reaches near-asymptotic performance at 20 components on our correlation metric.

(b) Dimensionality reduction of face embeddings via PCA. With EEG reduced to 20 D, the Linear Regression method reaches near-asymptotic performance at 10 components.

Figure 5: PCA component sweeps for (Left) EEG signals and (Right) face embeddings.

These analyses support our decision to reduce EEG data to 20 dimensions and face embeddings to 10 dimensions, as these choices balance dimensionality reduction with preservation of relevant information, as evidenced by the near-asymptotic performance in correlation metrics.

## C Experiments

### C.1 Comparative and ablation studies

**Estimators: Hyperparameters and Search.** We used default estimators’ meta-parameters with SVR using the radial basis function (RBF) kernel, and the MLP consisting of 3 hidden layers with (100, 50, and 25) neurons and a ReLU activation function. The learning rate for the MLP was set to 0.001, and the Adam optimizer used betas set at 0.9 and 0.999.

Additionally, we conducted an exhaustive hyperparameter search using “GridSearchCV” in scikit-learn [35] to optimize our Multi-Layer Perceptron (Best MLP) and SVR (Best SVR) models.

For the MLP estimator, we explored activation functions (Identity, ReLU), regularization parameter  $\alpha$  (0.0001, 0.01, 0.1, 1), hidden layer architectures ranging from simple (100), to comparatively more complex (1000, ..., 1000) up to 10 layers, and adaptive learning rates for all experiments. Models were evaluated using cross-validated mean RMSE scores.

For the SVR model, we explored the regularization parameter  $C$  (0.001, 0.01, 0.1, 1), kernel coefficient  $\gamma$  (“scale”, “auto”), and kernel type (linear, RBF). In total, 16 combinations were evaluated.

**Data and distance ablations.** We evaluated our algorithm performance with varying dataset sizes ( $N$ ) of [9234, 9000, 8000, 7000, 6000, 5000, 4000, 3000, 2000, 1000, 500, 100] to evaluate how the model performance is impacted by the amount of observed data. Each dataset was down-sampled to its final size using uniform random sampling without replacement.

We tested sensitivity to near-target stimuli by removing stimuli-response pairs below various distance thresholds from the target face [0, 5, 10, 15, 20, 25, 30, 35, 40]. This reduced dataset size to, respectively, [9234, 6644, 5432, 4335, 3413, 2668, 2047, 1452, 806]. To control for dataset size effects, we ran parallel experiments with uniformly down-sampled datasets matching each threshold’s size.

**Optimization ablation and control.** We conducted this ablation studies to investigate the importance of near-target stimuli on CURSOR’s performance. Because this removed data from the stimuli-response set, our experiment also impacted data scarcity. To control for dataset size effects, we ran control experiments with uniformly down-sampled datasets matching each near-target ablation threshold’s size. Figure 6 illustrates the results of these experiments (mean  $\pm$  SD, x-axis inverted).

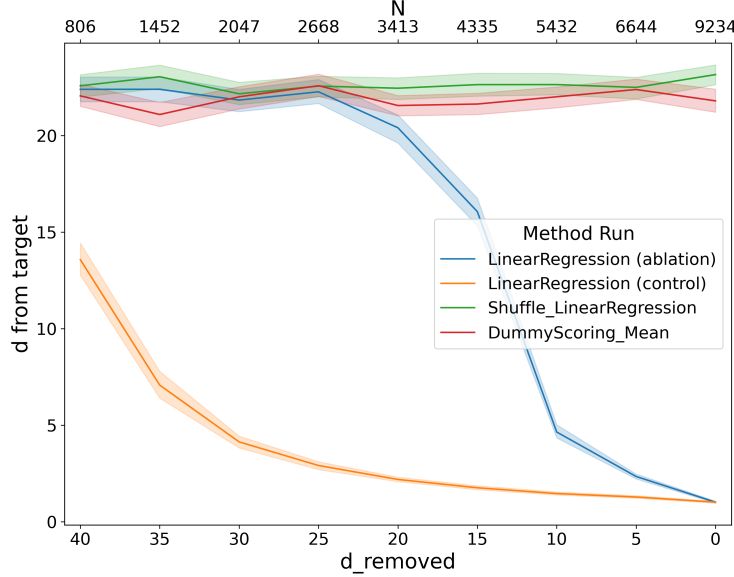


Figure 6: Comparison of CURSOR performance under near-target ablation and uniform data reduction conditions. Figure shows distance to target of candidates found after 1000 iterations against dataset ablated within specified distances  $d_{removed}$  around the target (mean  $\pm$  SD). We can recover near-target faces even when near-target stimuli are absent in the dataset, up to  $d_{removed} = 10$ , demonstrating CURSOR’s ability to infer beyond its observation space and its robustness to data scarcity. The disparity in performance between ablation and control conditions at comparable  $N$  values highlights the importance of near-target stimuli for CURSOR’s accuracy.

**Estimator performance on supervised tasks vs CURSOR Performance.** We trained various estimators on ground truth data to estimate their theoretical capacity for predicting  $d$  from  $e$ . The root mean square error (RMSE) is used as a performance metric, with lower values indicating better performance. The primary objective of this study is to investigate whether CURSOR’s effectiveness is dependent on having a highly accurate estimator, and to explore the relationship between the estimator’s capacity to capture data relationships and its performance within the CURSOR framework.

## C.2 Human validation experiments

***H-Rank* — Ranking face similarity with unlimited time.** The *H-Rank* experiment evaluates the ability to manually assign distance scores and rank images from single latent trajectories between the target and the farthest image used in the EEG experiment. An evaluator, uninvolved in the EEG experiment and sourced from a university population, was presented with sets of 10 progressively morphed images spanning distances from 0 to 40.16 ( $D = \{0, 1.6, 3.6, 6.8, 10.9, 16.3, 21.7, 29.4, 36.7, 46.2\}$ ) (Figure 2 right) and the scale was normalized between 0 and 1 for ease of evaluation. The remaining 8 images were unlabeled and displayed in a randomized order. The task was not timed, and all 10 images per set were displayed simultaneously. In total, the evaluator assessed 170 images, corresponding to 10 images per each of the 17 targets. An alternative representation of the results from the main paper is shown in Figure 7.

***H-ID* — Face identification from short exposure.** The *H-ID* experiment aims to contextualise our results by determining the distances in  $Z$  at which two faces are indistinguishable or become clearly differentiable by human evaluators.

During *H-ID* trials, a target face  $z^*$  was presented centrally for 1.5 s, followed by a 1-second blank interval. Then, two faces were displayed side-by-side for 0.5 s: the target face  $z^*$  and a comparison face  $z_c$  at a distance  $d_{z_c} = \rho_{z^*}(z_c)$  from the target. The 0.5 s exposure duration was chosen to match the stimulus presentation time used to acquire the dataset in our neurophysiological experiments. Participants were instructed to click on the face they believed matched the target face shown previously.

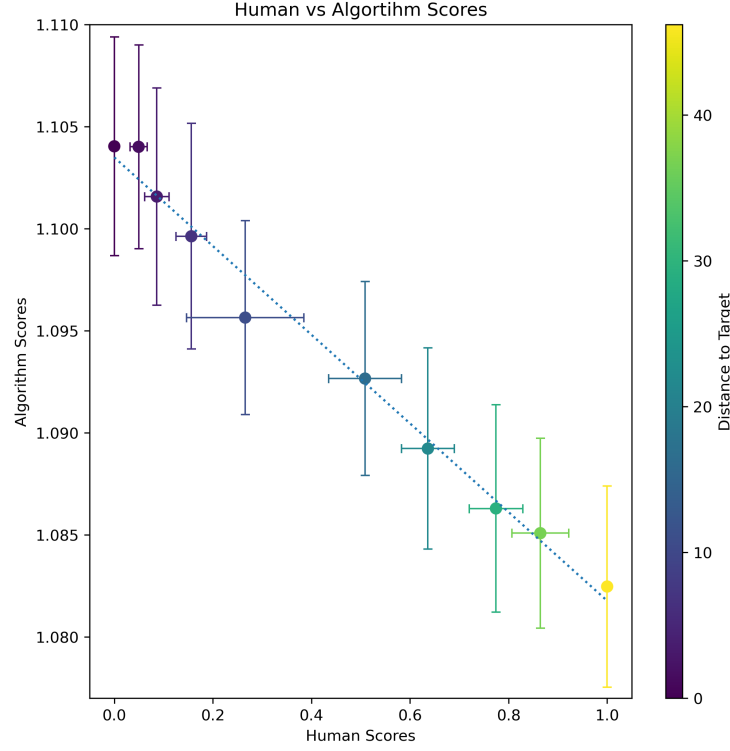


Figure 7: Human scores attached to a subset of test faces (unlimited time) vs Algorithm score from our method using Linear Regressor on full dataset (error bars show the standard deviation). Each dot represents a test face colored by the distance this face is from the target face. Our algorithms scores correlates strongly with human scores.

For each trial, the target face was selected randomly from the 17 target faces available in our dataset. The position of the target face in the selection stage (left or right) was randomized across trials. The distance  $d_{z_c}$  between the target and comparison face was randomly chosen within the  $D$  set as for *H-Rank*. Each participants completed 30 such trials. A local machine was used in the setup, using Flask as backend and HTML/CSS/JS for the frontend.

53 participants volunteered for the study, aged between 20 and 39 years (mean = 24.5, SD = 3), of which 8 self-identified female, 45 as male, and none as diverse. All participants were informed of the study’s purpose, reported no visual impairments, and provided written consent before participation.

We calculated the identification error rate  $\eta(d_{z_c})$  as the proportion of incorrect selections at each distance  $d_{z_c}$ , using Wilson score for confidence intervals. At  $d_{z_c} = 0$ , we expect chance performance (error rate 0.5), while for clearly differentiable faces, the error rate should approach 0. *H-ID* was designed to reveal the transition between these extremes.

### C.3 Computational environment

The computations were performed locally on GNU/Linux and MacOS-based machines:

- A Lenovo Thinkpad t480 running Ubuntu 22.04, an i5-7300U Intel CPU at a base frequency of 2.6 GHz, Intel HD Graphics 620, and 32GB / 2400MHz DDR4 RAM;
- A custom machine running Linux 6.10.3, an AMD Ryzen 7 7840U 16 core at a base frequency of 3.3 GHz with Radeon 780M Graphics, and 64 GB / DDR5-5600 RAM;
- A MacBookPro running MacOS Sonoma 14.3, an Apple M1 Max with 10 cores and 64GB RAM.

Most computationally intensive tasks were executed on an on-premises AlmaLinux 8.7 cluster with a SLURM scheduler and AMD EPYC 7452 CPUs. Computations utilized embarrassingly parallel tasks, each running on a single CPU core. Jobs were run on nodes designated for “short” or “medium” tasks, suggesting relatively low HPC resource demands per job. We launched one job array per estimator due to varying resource requirements. Initial computational load was assessed with a job configuration of 1 CPU core, 800 MB of RAM, and a walltime of 1 hour, and adjusted based on observed resource usage. Maximum RAM usage and walltime, with at least a 20% buffer for variability, were 400 MB and 4 hours for Linear Regression, 400 MB and 4 hours for MLP, and 600 MB and 15 hours for SVR.

There are no specific package version requirements. We use Python 3.11, the oldest stable version at submission time supporting advanced enumerations for quality of life improvements, and therefore dependency versions are flexible. Details on the packages can be found in the dependencies file in the code.

## D Alternative EEG Representations

EEGNet model was trained on a separate dataset specifically for visual saliency detection using P3-based binary *classification*. The EEG data was collected using the same equipment and GAN as in the main experiment to minimize confounds, drift, and noise differences.

### D.1 Neurophysiological experiment for visual saliency in faces

After obtaining approval from the Ethical Committee of ANONYMOUS INSTITUTION, we recruited 31 participants from a University population. Images were generated using the same GAN architecture trained on a dataset of celebrity faces as in the main experiment, sampled from a 512-dimensional multivariate normal distribution. These images were manually categorized into eight visual categories: blond, dark-haired, female, male, old, young, smiling, and non-smiling. The study apparatus, including the EEG recording setup and stimuli presentation, was consistent with the main experiment.

After providing informed consent, participants were instructed to identify whether each face shown in a rapid serial visual presentation (RSVP) sequence of 70 images contained one of the eight salient features (*target*) while maintaining a mental count. Each salient feature was presented in 4 RSVP trials before switching to the next category. The order of target and non-target images was randomized, as in the main experiment.

Following data collection, EEG data was preprocessed offline using a high-pass filter at 0.2 Hz and a low-pass filter at 35 Hz. The data was then epoched and baselined as in the main experiment, with artifacts removed using a threshold of  $\pm 400 \mu\text{V}$  based on the highest absolute maximum voltage. This preprocessing step removed two participants due to artifacts and approximately 11% of epochs, resulting in a dataset with an average of 3251 epochs per participant.

### D.2 Learning task and prediction setup

EEGNet models were trained to classify the presence or absence of salient features in face images. Each model utilized EEG epochs containing 29 channels and 376 time points as input, with a binary classification label as the output. The training process spanned 10 epochs with a batch size of 32, employing a binary cross-entropy loss and the Adam optimizer with a learning rate of 0.001 and moment betas set to 0.9 and 0.999. For evaluation, data corresponding to one salient visual category was left out during training. After training, the final classification layer of the EEGNet model was removed, and the remaining network was used to generate embeddings using EEG data from the main experiment as input.

## E Results

### E.1 Comparative and ablation studies

**Estimators: Hyperparameter search.** We ran hyperparameter optimization to identify the best-performing MLP and SVR models for the CURSOR framework (“Best MLP” and “Best SVR”).

For the Best MLP model, identity activation generally outperformed ReLU, with moderate alpha values (0.1) yielding better results. Simpler architectures (2–3 layers) often performed comparably to or better than more complex ones. The best-performing configuration consisted of identity activation,  $\alpha = 0.1$ , and two hidden layers of size 100 with an adaptive learning rate. This configuration achieved a mean RMSE score of  $0.9138 \pm 0.0142$  (mean  $\pm$  SD).

For the Best SVR model, linear kernels outperformed RBF kernels. Performance was relatively stable across  $C$  values for linear kernels, with the best performance at  $C = 0.01$ . The “scale” and “auto”  $\gamma$  settings produced identical results for linear kernels. RBF kernels showed lower performance, suggesting linear separability in the feature space. The best-performing configuration was  $C = 0.01$ ,  $\gamma = \text{“scale”}$ , and the linear kernel, achieving a mean RMSE score of  $0.9279 \pm 0.0115$  (mean  $\pm$  SD).

## E.2 Estimator performance on supervised tasks vs. CURSOR performance

**Aligned vs. Shuffled Performance.** Figure 8 presents a scatter plot comparing the RMSE of each estimator on aligned and shuffled datasets. Baseline methods exhibit equal performance on both datasets, as expected. Despite displaying the lowest absolute performance, the MLP shows relative improvement over the shuffled dataset, allowing it to outperform baselines with better absolute RMSE scores in the CURSOR framework. This finding suggests that CURSOR’s effectiveness is not solely dependent on having the best possible estimator in absolute performance.

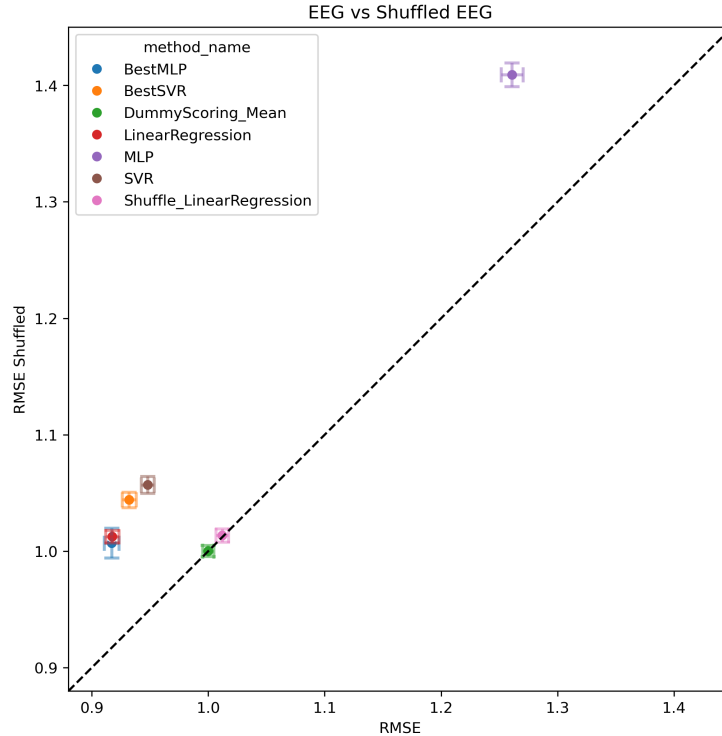


Figure 8: Comparison of estimator performance on aligned vs. shuffled EEG data. The x-axis shows the RMSE on aligned data, while the y-axis shows the RMSE on shuffled data. Each point represents a different estimator, with error bars indicating standard deviation. The diagonal dashed line represents equal performance on both datasets. Points above this line indicate better performance on aligned data compared to shuffled data, which is desirable for CURSOR. Note that while some methods (e.g., MLP) may have higher absolute RMSE, they still show improvement over the shuffled baseline, demonstrating potential utility in the CURSOR framework.

**RMSE vs. Pearson Correlation.** Figure 9 illustrates the relationship between estimator performance on ground truth data and the Pearson correlation statistic for the information retrieval (IR) task. The Best SVR model achieves a lower RMSE than the standard SVR but demonstrates lower

performance in ranking correlation with ground truth distances. The MLP performs nearly as well as the Best SVR in the CURSOR framework despite a substantial difference in RMSE. This counterintuitive result is possible due to CURSOR’s scoring function, which measures relative improvement. Further investigation into the mechanisms behind this phenomenon could yield valuable insights.

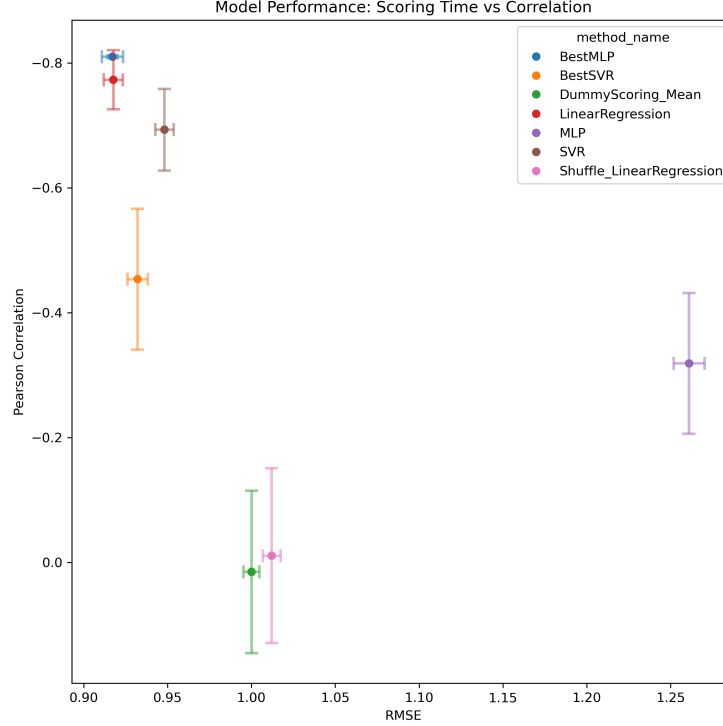


Figure 9: Relationship between estimator performance and CURSOR effectiveness. The x-axis shows the RMSE of each estimator on the target face dataset (lower is better), while the y-axis shows the Pearson correlation between the estimator’s rankings and ground truth distances (higher absolute value is better). Each point represents a different estimator method, with error bars indicating standard deviation. Notably, methods with similar RMSE can have vastly different correlations, and some methods with higher RMSE (e.g., MLP) can achieve correlations comparable to methods with lower RMSE (e.g., BestSVR). This demonstrates that absolute estimator performance does not necessarily predict effectiveness within the CURSOR framework.

**Conclusions.** The relationship between estimator characteristics and CURSOR performance is complex, unlike typical supervised or unsupervised learning scenarios. These findings argue for ensemble methods that dynamically test different estimators within the CURSOR framework. Future research should focus on developing robust confidence metrics for CURSOR scores estimations.

In conclusion, this study reveals the complex interplay between estimator characteristics and CURSOR performance. The framework’s ability to extract useful information from estimators with suboptimal absolute performance highlights its robustness and adaptability. These findings open avenues for future research, particularly in dynamic estimator selection strategies and improved confidence estimation techniques.

### E.3 Ranking images and optimizing the image embedding

Images ranked and generated for the 17 targets are shown in Figure 10. Table 2 extends the main paper’s results for EEG preprocessing using windowing (left) and includes a subset re-run using EEGNet embeddings (right). Trends and magnitudes are aligned between the two EEG representations, suggesting EEGNet embeddings as an alternative preprocessing method in the CURSOR framework. This allows us to provide embeddings as attached data, overcoming the challenge of sharing raw EEG data.





Table 2: Euclidean distance ( $d$ ) at the top rank, coefficient of determination (R), and rank shown as mean  $\pm$  standard deviation for each estimator: linear regression (LR), shuffled linear regression (S-LR), dummy scoring mean, default and optimized (“best”) multi-layer perceptron (MLP), and default and best support vector regression (SVR). Results are presented for two alternative EEG representations: one applying windowing over the raw signal, and the other using EEGNet embeddings.

Regressor	EEG windowing			EEGNet		
	$d$ top rank	R	Rank	$d$ top rank	R	Rank
LR	2.90 $\pm$ 3.08	-0.77 $\pm$ 0.04	6.63 $\pm$ 5.75	2.66 $\pm$ 3.02	-0.76 $\pm$ 0.05	6.21 $\pm$ 6.03
S-LR	20.85 $\pm$ 13.48	-0.01 $\pm$ 0.14	27.13 $\pm$ 18.45	21.07 $\pm$ 13.73	-0.01 $\pm$ 0.13	26.35 $\pm$ 16.93
Dummy	21.97 $\pm$ 12.86	0.01 $\pm$ 0.13	27.91 $\pm$ 15.95	22.29 $\pm$ 12.44	-0.01 $\pm$ 0.14	27.73 $\pm$ 16.60
MLP	12.11 $\pm$ 11.07	-0.32 $\pm$ 0.11	21.68 $\pm$ 15.48	13.26 $\pm$ 11.46	-0.31 $\pm$ 0.11	19.85 $\pm$ 15.01
BestMLP	4.30 $\pm$ 2.64	-0.81 $\pm$ 0.00	9.67 $\pm$ 10.02	3.91 $\pm$ 3.53	-0.76 $\pm$ 0.04	6.14 $\pm$ 5.89
SVR	6.77 $\pm$ 4.65	-0.69 $\pm$ 0.06	16.04 $\pm$ 10.38	6.12 $\pm$ 4.61	-0.69 $\pm$ 0.06	15.65 $\pm$ 12.85
BestSVR	12.60 $\pm$ 5.53	-0.45 $\pm$ 0.11	43.34 $\pm$ 13.37	13.17 $\pm$ 4.48	-0.40 $\pm$ 0.12	44.86 $\pm$ 13.88

#### E.4 Computation time vs. performance

Figure 11 examines the relationship between computation time and performance. The primary observation is the marked variability in computation time among methods. Given the weak correlation between performance and computation time, it may be advantageous to initially focus on faster-to-train estimators when implementing CURSOR.

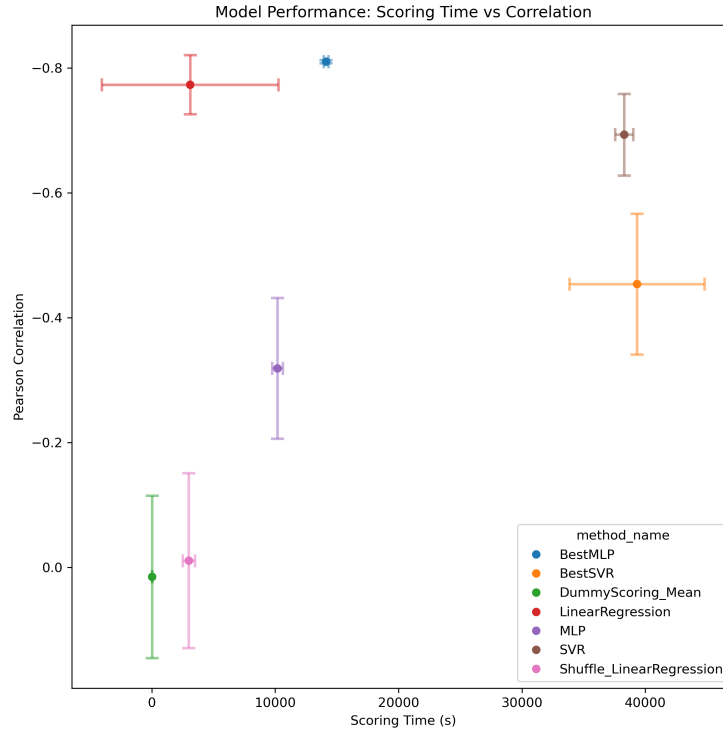


Figure 11: Trade-off between computational time and performance in the CURSOR framework. The x-axis shows the scoring time in seconds, while the y-axis shows the Pearson correlation between the estimator’s rankings and the ground truth distances. Each point represents a different estimator, with error bars indicating standard deviation.



## E.5 Optimization ablation and control

Our primary finding is that CURSOR can recover a target face within  $d < 5$  even when no stimuli within  $d < 10$  have been observed. This demonstrates CURSOR’s ability to infer beyond its current observation space, a crucial feature for practical applications where near-target stimuli may be scarce.

Comparing the ablation and control conditions reveals the significant impact of near-target stimuli on performance. When  $d_{removed} > 10$ , CURSOR was unable to recover a face at  $d < 5$  from the target, even with  $N = 5432$  stimuli-response pairs. In contrast, under uniform data reduction (control condition), similar performance was achievable with only  $N = 2047$  pairs.

This performance disparity at comparable  $N$  values confirms that responses to stimuli close to the target significantly enhance CURSOR’s accuracy. It suggests that strategic sampling, informed by CURSOR scores could potentially improve the efficiency of the algorithm in practical scenarios and is worth further research. These results highlight CURSOR’s robustness to data scarcity and its ability to perform well even with limited near-target information, while also emphasizing the value of near-target stimuli for optimal performance.

## E.6 Recovering ground-truth labels.

Using the best stimuli  $\hat{h}$  identified during the optimization process, we reconstructed labels for each observed response  $e_i$  as the distance  $d_i^{\hat{h}} = \rho_{\hat{h}}(z_i)$ . The quality of these reconstructed labels is measured by their RMSE compared to the ground-truth labels  $d^{z^*}$ . For LR,  $\text{RMSE}(d^{z^*}, d^{\hat{h}})$  is  $0.18 \pm 0.08$ , representing less than 0.4% of the range of  $d$  values and outperforming S-LR at  $15.20 \pm 3.21$  and Dummy at  $18.23 \pm 2.99$  (both Mann-Whitney U,  $p < 0.001$ , Bonferroni corrected). It demonstrates our method’s ability to recover ground-truth labels without supervision and suggests potential effectiveness in downstream tasks requiring labels comparable to calibrated approaches.

# F Discussion, Limitations and Conclusions

## F.1 Limitations.

Our findings should be replicated in online settings using protocols matching our simulations. This might surface additional constraints for practical deployment. For example, prolonged or repeated exposure might attenuate the P3 response, potentially affecting the system’s reliability [1, 6]. Active sampling might also help reduce the amount of EEG-stimuli pairs required, which is currently a major limitation to practical use.

## F.2 Ethical implications and potential applications.

Ethical considerations are crucial in this line of research as the ability to infer people’s intent without explicit questioning or consent raises important privacy and ethical concerns that warrant caution of application scenarios [9, 11]. Potential negative societal impacts, due to performance instability in risk-sensitive applications, need to be carefully addressed. Working on explainable SC-BCIs and methods to assess confidence of their predictions will play a crucial role.

Despite potential risks, this technology could have beneficial applications, particularly in diagnostic scenarios where user feedback is unreliable or calibration is difficult, such as early diagnosis of neurodegenerative disorders [36]. Future research should explore such positive use cases while remaining vigilant about potential misuse.

## References

- [1] Hamad Ahmed et al. “Confounds in the Data—Comments on “Decoding Brain Representations by Multimodal Learning of Neural Activity and Visual Features””. In: *IEEE Transactions on Pattern Analysis and Machine Intelligence* 44.12 (2022), pp. 9217–9220. DOI: 10.1109/TPAMI.2021.3121268.
- [2] Hamad Ahmed et al. “Object Classification From Randomized EEG Trials”. In: *Proceedings of the IEEE/CVF Conference on Computer Vision and Pattern Recognition (CVPR)*. June 2021, pp. 3845–3854.
- [3] Takuya Akiba et al. *Optuna: A Next-generation Hyperparameter Optimization Framework*. 2019. arXiv: 1907.10902 [cs.LG].
- [4] Yunpeng Bai et al. “Dreamdiffusion: Generating high-quality images from brain EEG signals”. In: *arXiv preprint arXiv:2306.16934* (2023).
- [5] Paul Barde et al. *Learning to Guide and to Be Guided in the Architect-Builder Problem*. 2022. arXiv: 2112.07342 [cs.LG].
- [6] Hari M Bharadwaj, Ronnie B. Wilbur, and Jeffrey Mark Siskind. “Still an Ineffective Method With Supertrials/ERPs—Comments on “Decoding Brain Representations by Multimodal Learning of Neural Activity and Visual Features””. In: *IEEE Transactions on Pattern Analysis and Machine Intelligence* 45.11 (2023), pp. 14052–14054.
- [7] Benjamin Blankertz. “Gentle introduction to signal processing and classification for single-trial EEG analysis”. In: *Brain–Computer Interfaces Handbook*. CRC Press, 2018, pp. 343–370.
- [8] Benjamin Blankertz et al. “Single-trial analysis and classification of ERP components — A tutorial”. In: *NeuroImage* 56.2 (2011). Multivariate Decoding and Brain Reading, pp. 814–825. ISSN: 1053-8119. DOI: 10.1016/j.neuroimage.2010.06.048.
- [9] Keith Davis and Tuukka Ruotsalo. “Physiological Data: Challenges for Privacy and Ethics”. In: *arXiv preprint arXiv:2405.15272* (2024).
- [10] Lawrence A. Farwell and Emanuel Donchin. “Talking off the top of your head: toward a mental prosthesis utilizing event-related brain potentials”. In: *Electroencephalography and clinical Neurophysiology* 70.6 (1988), pp. 510–523. DOI: 10.1016/0013-4694(88)90149-6.
- [11] Lawrence A. Farwell and Emanuel Donchin. “The Truth Will Out: Interrogative Polygraphy (“Lie Detection”) With Event-Related Brain Potentials”. In: *Psychophysiology* 28.5 (1991), pp. 531–547. DOI: 10.1111/j.1469-8986.1991.tb01990.x.
- [12] Alessandro T. Gifford et al. “A large and rich EEG dataset for modeling human visual object recognition”. In: *NeuroImage* 264 (2022), p. 119754. ISSN: 1053-8119. DOI: 10.1016/j.neuroimage.2022.119754.
- [13] Ian J. Goodfellow et al. “Generative Adversarial Nets”. In: *Proc. NIPS*. 2014, pp. 2672–2680.
- [14] Alexandre Gramfort et al. “MEG and EEG Data Analysis with MNE-Python”. In: *Frontiers in Neuroscience* 7.267 (2013), pp. 1–13. DOI: 10.3389/fnins.2013.00267.
- [15] Jonathan Grizou. *Interactive introduction to self-calibrating interfaces*. 2022. arXiv: 2212.05766 [cs.HC].
- [16] Jonathan Grizou, Manuel Lopes, and Pierre-Yves Oudeyer. “Robot learning simultaneously a task and how to interpret human instructions”. In: *2013 IEEE third joint international conference on development and learning and epigenetic robotics (ICDL)*. IEEE. 2013, pp. 1–8.
- [17] Jonathan Grizou et al. “Calibration-free BCI based control”. In: *Proceedings of the AAAI Conference on Artificial Intelligence*. Vol. 28. 2014.
- [18] Tijl Grootswagers et al. “Human EEG recordings for 1,854 concepts presented in rapid serial visual presentation streams”. In: *Scientific Data* 9.1 (2022), p. 3. ISSN: 2052-4463. DOI: 10.1038/s41597-021-01102-7.
- [19] Sven Guenther, Nataliya Kosmyna, and Pattie Maes. “Image classification and reconstruction from low-density EEG”. In: *Scientific Reports* 14.1 (July 2024), p. 16436. ISSN: 2045-2322. DOI: 10.1038/s41598-024-66228-1.
- [20] Nikolaus Hansen. “The CMA evolution strategy: a comparing review”. In: *Towards a new evolutionary computation: Advances in the estimation of distribution algorithms* (2006), pp. 75–102.
- [21] David Hübner et al. “Learning from label proportions in brain-computer interfaces: Online unsupervised learning with guarantees”. In: *PloS one* 12.4 (2017), e0175856.

- [22] David Hübner et al. “Unsupervised learning for brain-computer interfaces based on event-related potentials: Review and online comparison [research frontier]”. In: *IEEE Computational Intelligence Magazine* 13.2 (2018), pp. 66–77.
- [23] Iñaki Iturrate et al. “Exploiting task constraints for self-calibrated brain-machine interface control using error-related potentials”. In: *PloS one* 10.7 (2015), e0131491.
- [24] Mainak Jas et al. “Automated rejection and repair of bad trials in MEG/EEG”. In: *2016 International Workshop on Pattern Recognition in Neuroimaging (PRNI)*. 2016, pp. 1–4. DOI: 10.1109/PRNI.2016.7552336.
- [25] Mainak Jas et al. “Autoreject: Automated artifact rejection for MEG and EEG data”. In: *NeuroImage* 159 (2017), pp. 417–429. ISSN: 1053-8119. DOI: 10.1016/j.neuroimage.2017.06.030.
- [26] Lauri Kangassalo, Michiel Spapé, and Tuukka Ruotsalo. “Neuroadaptive modelling for generating images matching perceptual categories”. In: *Scientific Reports* 10.1 (2020), p. 14719. ISSN: 2045-2322. DOI: 10.1038/s41598-020-71287-1.
- [27] Tero Karras et al. “Progressive Growing of GANs for Improved Quality, Stability, and Variation”. In: *Proc. ICLR*. 2018.
- [28] Pieter-Jan Kindermans, David Verstraeten, and Benjamin Schrauwen. “A bayesian model for exploiting application constraints to enable unsupervised training of a P300-based BCI”. In: *PloS one* 7.4 (2012), e33758.
- [29] Vernon J Lawhern et al. “EEGNet: a compact convolutional neural network for EEG-based brain–computer interfaces”. In: *Journal of neural engineering* 15.5 (2018), p. 056013.
- [30] Steven Lemm et al. “Introduction to machine learning for brain imaging”. In: *NeuroImage* 56.2 (2011). Multivariate Decoding and Brain Reading, pp. 387–399. ISSN: 1053-8119. DOI: 10.1016/j.neuroimage.2010.11.004.
- [31] Ren Li et al. “The Perils and Pitfalls of Block Design for EEG Classification Experiments”. In: *IEEE Transactions on Pattern Analysis and Machine Intelligence* 43.1 (2021), pp. 316–333. DOI: 10.1109/TPAMI.2020.2973153.
- [32] Kathryn McConkey et al. *IFTT-PIN: A Self-Calibrating PIN-Entry Method*. 2024. arXiv: 2407.02269 [cs.HC].
- [33] Kento Nozawa and Issei Sato. “Empirical evaluation and theoretical analysis for representation learning: A survey”. In: *arXiv preprint arXiv:2204.08226* (2022).
- [34] L. C. Parra et al. “Recipes for the linear analysis of EEG”. In: *Neuroimage* 28.2 (Nov. 2005), pp. 326–341. DOI: 10.1016/j.neuroimage.2005.05.032.
- [35] F. Pedregosa et al. “Scikit-learn: Machine Learning in Python”. In: *Journal of Machine Learning Research* 12 (2011), pp. 2825–2830.
- [36] María Luisa Barragán Pulido et al. “Alzheimer’s disease and automatic speech analysis: a review”. In: *Expert systems with applications* 150 (2020), p. 113213.
- [37] Novi Quadrianto et al. “Estimating labels from label proportions”. In: *Proceedings of the 25th international conference on Machine learning*. 2008, pp. 776–783.
- [38] Siddharth Reddy, Sergey Levine, and Anca Dragan. “First contact: Unsupervised human-machine co-adaptation via mutual information maximization”. In: *Advances in Neural Information Processing Systems* 35 (2022), pp. 31542–31556.
- [39] Robin Tibor Schirrmeister et al. “Deep learning with convolutional neural networks for EEG decoding and visualization”. In: *Human Brain Mapping* (Aug. 2017). ISSN: 1097-0193. DOI: 10.1002/hbm.23730.
- [40] Jan Sosulski and Michael Tangermann. “UMM: Unsupervised mean-difference maximization”. In: *arXiv preprint arXiv:2306.11830* (2023).
- [41] Michiel Spapé, Rinus Verdonchot, and Henk van Steenbergen. *The E-Primer: An introduction to creating psychological experiments in E-Prime. Second edition updated for E-Prime 3*. 2nd ed. Leiden, The Netherlands: Leiden University Press, 2019.
- [42] Abdulhamit Subasi and M. Ismail Gursoy. “EEG signal classification using PCA, ICA, LDA and support vector machines”. In: *Expert Systems with Applications* 37.12 (2010), pp. 8659–8666. ISSN: 0957-4174. DOI: 10.1016/j.eswa.2010.06.065.
- [43] Jordy Thielen, Jan Sosulski, and Michael Tangermann. “Learning to walk on new ground: Calibration-free decoding for c-VEP BCI”. In: *arXiv preprint arXiv:2403.15521* (2024).

- [44] C. de la Torre-Ortiz and T. Ruotsalo. “Perceptual Visual Similarity from EEG: Prediction and Image Generation”. In: *Proceedings of the 32nd ACM International Conference on Multimedia (MM '24)*. Melbourne, VIC, Australia: ACM, 2024, October 28–November 1. ISBN: 979-8-4007-0686-8/24/10. DOI: 10.1145/3664647.3685508.
- [45] C. de la Torre-Ortiz, M. Spapé, and T. Ruotsalo. “The P3 indexes the distance between perceived and target image”. In: *Psychophysiology* 60.5 (May 2023), e14225.
- [46] Thibault Verhoeven et al. “Improving zero-training brain-computer interfaces by mixing model estimators”. In: *Journal of neural engineering* 14.3 (2017), p. 036021.
- [47] Anna-Lisa Vollmer et al. “Studying the co-construction of interaction protocols in collaborative tasks with humans”. In: *4th International Conference on Development and Learning and on Epigenetic Robotics*. IEEE. 2014, pp. 208–215.
- [48] Guangyu Wang et al. “EEGPT: Pretrained Transformer for Universal and Reliable Representation of EEG Signals”. In: *The Thirty-eighth Annual Conference on Neural Information Processing Systems*. 2024.
- [49] William F Whitney et al. “Evaluating representations by the complexity of learning low-loss predictors”. In: *arXiv preprint arXiv:2009.07368* (2020).
- [50] John Williamson and Roderick Murray-Smith. “Pointing without a pointer”. In: *CHI'04 Extended Abstracts on Human Factors in Computing Systems*. 2004, pp. 1407–1410.
- [51] Tengyang Xie et al. “Interaction-grounded learning with action-inclusive feedback”. In: *Advances in Neural Information Processing Systems* 35 (2022), pp. 12529–12541.